RESEARCH ARTICLE

Dispersal and air entrainment in unconfined dilute pyroclastic density currents

Benjamin J. Andrews

Abstract Unconfined scaled laboratory experiments show that 3D structures control the behavior of dilute pyroclastic density currents (PDCs) during and after liftoff. Experiments comprise heated and ambient temperature 20 μm talc powder turbulently suspended in air to form density currents within an unobstructed 8.5×6×2.6-m chamber. Comparisons of Richardson, thermal Richardson, Froude, Stokes, and settling numbers and buoyant thermal to kinetic energy densities show good agreement between experimental currents and dilute PDCs. The experimental Reynolds numbers are lower than those of PDCs, but the experiments are fully turbulent; thus, the large-scale dynamics are similar between the two systems. High-frequency, simultaneous observation in three orthogonal planes shows that the currents behave very differently than previous 2D (i.e., confined) currents. Specifically, whereas ambient temperature currents show radial dispersal patterns, buoyancy reversal, and liftoff of heated currents focuses dispersal along narrow axes beneath the rising plumes. The aspect ratios, defined as the current length divided by a characteristic width, are typically 2.5–3.5 in heated currents and 1.5–2.5 in ambient temperature currents, reflecting differences in dispersal between the two types of currents. Mechanisms of air entrainment differ greatly between the two currents: entrainment occurs primarily behind the heads and through the upper margins of ambient temperature currents, but heated currents entrain air through their lateral margins. That lateral entrainment is much more efficient than the vertical entrainment, >0.5 compared to ~0.1, where entrainment is defined as the ratio of cross-stream to streamwise velocity. These experiments suggest that generation of coignimbrite plumes should focus PDCs along narrow transport axes, resulting in elongate rather than radial deposits.

Keywords Pyroclastic density currents · Experimental volcanology · Entrainment · Explosive volcanism

Introduction

Dilute particle-laden density currents are common phenomena in a range of geological settings, including powder snow avalanches, turbidity currents, and pyroclastic density currents (PDCs). The latter two types of sediment gravity flows can distribute material over thousands of square kilometers through direct deposition from the currents, and, in the case of PDCs, through buoyancy reversal and deposition of coignimbrite ash (e.g., Sigurdsson and Carey 1989; Fisher et al. 1993; Bursik and Woods 1996). PDCs also pose substantial hazards to life and property as they are fast and highly mobile (Dade and Huppert 1996; Fujii and Nakada 1999; Gardner et al. 2007; Druitt et al. 2002; Dellino and La Volpe 2000; Dellino et al. 2010; Cronin et al. 2013).

A large body of research from the sedimentology, fluid dynamics, and engineering communities describes dilute density currents. In general, the behavior of currents is controlled by their thickness, density contrast relative to the ambient fluid, and their duration (e.g., Dade and Huppert 1995a, b; Wells et al. 2010). Current density is controlled primarily by suspended particle concentration; particle sedimentation (or entrainment from the substrate) and ambient fluid entrainment change that concentration through time and space. Turbulence within currents promotes fluid and substrate particle entrainment, and the ratio of particle fall velocity to the turbulent

B. J. Andrews (✉)
Global Volcanism Program, Smithsonian Institution,
Washington, DC, USA
e-mail: andrewsb@si.edu

component of velocity helps to describe whether particles will sediment (e.g., Dade and Huppert 1995b; Burgisser et al. 2005; Cantero et al. 2012). Taken together, those relationships can provide elegant models that describe velocity, runout distance, and sedimentation (e.g., Dade and Huppert 1995a).

Many of the existing models for dilute density currents are derived from 1D approximations of the currents (e.g., Dade and Huppert 1995a, b such models are radially or axially symmetric. Most of the models rely either explicitly or implicitly on non-entrainment of the ambient fluid. In general, fluid entrainment results in a decrease in current density accompanied by a proportional increase in current thickness. Propagation speed scales with the square root of current thickness, h, times the density anomaly, g', as described by the Froude number, Fr:

$$ \mathrm{Fr} = \frac{U}{\sqrt{g'h}} $$

Because the density anomaly and thickness covary, the entrainment of ambient fluid in effectively isothermal systems results in little change to current velocity. Importantly, current density remains greater than ambient fluid density even for large amounts of entrainment (e.g., Wells et al. 2010; Stagnaro and Bolla Pittalyga 2013).

Unlike other dilute density currents, dilute PDCs are hot (typically >200–400 °C) and have large amounts of excess thermal energy available for conversion to kinetic energy or gravitational potential energy. As PDCs entrain much cooler ambient air, they heat and expand that air. Consequently, although the initial density of dilute PDCs is greater than the atmosphere (commonly 4–8 kg/m^3 compared to ~1.21 kg/m^3), air entrainment and expansion can drive current density to <1 kg/m^3, resulting in buoyancy reversal and current liftoff (Bursik and Woods 1996). Generation of buoyant, coignimbrite plumes is common, even from small PDCs, and indeed, the largest tephra fall deposits were dispersed by coignimbrite plumes rising from voluminous PDCs, not by plumes sourced directly above the eruption vent (Sigurdsson and Carey 1989; Woods and Kienle 1994; Bursik and Woods 1996; Fisher et al. 1993; Wilson 2008). Understanding air entrainment and expansion is thus vital to predicting the behavior of dilute PDCs.

Numerous studies of dilute density currents describe entrainment, but those studies generally have two shortcomings as applied to PDCs. First, the majority of previous density current experiments were conducted in aqueous systems (e.g., Bursik and Woods 2000; Wells et al. 2010; Stagnaro and Bolla Pittalyga 2013), and thus, the complex relationships between entrainment, thermal expansion, and buoyancy reversal could not be examined. Second, most experiments were conducted in 2D channels (e.g., Bursik and Woods 2000; Wells et al. 2010; Andrews and Manga 2011, 2012; Stagnaro and Bolla

Pittalyga 2013); that geometry allows for excellent visualization but permits no significant cross-channel motions or entrainment through currents' lateral margins. Numerical models provide useful insights into transport and depositional processes in PDCs, but models examining the multiphase turbulent dynamics of PDCs are computationally expensive (e.g., Dufek and Bergantz 2007; Esposti Ongaro et al. 2008). To make numerical models computationally practical, many models are 2D (e.g., Esposti Ongaro et al. 2002; Todesco et al. 2002) or model only a limited sector of 3D space (e.g., Dufek and Bergantz 2007), but such approximations may fail to capture important dynamics that only manifest in three dimensions.

This paper presents experimental results describing the 3D structure and dynamics of dilute density currents. In particular, the study quantifies the turbulent entrainment in currents with and without reversing buoyancy and shows that variations in entrainment through space and time control current behavior. This work shows that currents focus along narrow transport axes when buoyancy reversal begins, and thus, radially symmetric models are not appropriate for density currents that evolve buoyant plumes and entrainment in three dimensions must be accounted for in numerical models of dilute PDCs.

Experimental and analytical methods

Experimental density currents comprising particles turbulently suspended in air were generated in a laboratory at the Smithsonian Institution Museum Support Center in Suitland, MD. The experimental apparatus, hereafter referred to as "the tank" (Fig. 1), has unobstructed interior dimensions 8.5 m long, 6 m wide, and 2.6 m tall. The tank is air-filled and in communication with the room; it is not air-tight but contains the particles and creates a still environment for experiments. Windows are installed along one side and the upstream end to allow observation. Twenty-micrometer talc particles similar to those used by Andrews and Manga (2011, 2012) were used in the experiments. The particles can be heated to generate currents with thermal scaling dynamically similar to natural dilute PDCs.

Laboratory currents are created following a method similar to that described by Andrews and Manga (2011, 2012). Briefly, currents are generated by loading a known mass of particles onto a measured length of conveyor belt. The particles composing warm currents are heated in an oven prior to loading. The conveyor belt is then run at a known speed such that the particles fall down a chute into the tank at a known rate. Most of the mass introduced to the tank remains on a pad at the base of the chute, but 3–10 % of the mass mixes with air as it enters the tank as a turbulent, particle-laden density current. The current mass is taken as the difference between the initial mass loaded onto the conveyor and the mass emplaced on the pad at
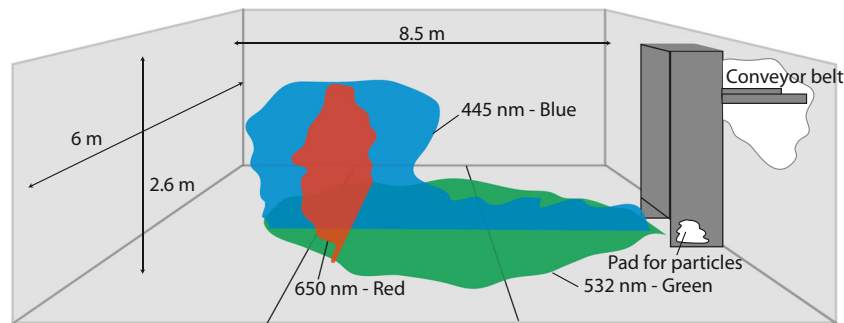
Fig. 1 Cartoon illustrating the experimental apparatus at the Smithsonian Institution Museum Support Center. The "tank" measures 8.5×6×2.6 m. Powder is loaded onto a conveyor belt that extends out the upstream side of the tank, and that conveyor then supplies powder at a known rate down a chute and into the tank; particles that do not form currents are collected on a pad at the base of the chute. Currents are illuminated by three orthogonal laser sheets: vertical sheets are oriented in the streamwise (*blue*) and cross-stream (*red*) planes, and a green sheet illuminates the horizontal plane at a height of 10 cm. Currents are recorded with an array of HD video cameras, and temperature is monitored with an array of thermal resistors

the base of the chute. The average rate at which currents are fed is the quotient of the current mass and duration over which particles are introduced to the tank.

Temperature within the tank is monitored with thermal resistors mounted in the mouth of the chute, 5 cm above the tank floor in the path of the current, and along one wall. Those probes measure the initial current temperature, the temperature of the current 2 m from the chute, and thermal stratification within the tank. The sensors are accurate to 0.1 °C, and data are logged at 10 Hz to a computer. The time constant of those sensors is ~2 s; thus, the temperature record is oversampled.

The currents are illuminated using three orthogonal laser sheets that span the full dimensions of the tank; the test section is thus the entire tank. A 650-nm red sheet generated by five 300-mW lasers is oriented vertically in the cross-stream direction 3 m from the mouth of the chute. A 532-nm green laser sheet generated by five 250-mW lasers is oriented horizontally 10 cm above the tank floor. A 445-nm laser sheet generated by five 400-mW blue lasers is oriented vertically along the streamwise centerline.

Four HD video cameras (Canon Vixia HF-100) and three DSLR cameras (Canon T2i and T3i with 18–55 and 18–70 mm lenses) record experiments at 30 frames per second through windows along the side and upstream end of the tank. Those cameras utilize CMOS sensors whose pixels are grouped in 2×2 clusters with peak sensitivities at ~530 (2 pixels), ~650, and ~450 nm; thus, although the sensors have nominally 1,920×1,080 resolution, the independent resolution is 960×540. The sensitivities of the pixels match the wavelengths of the laser sheets; by splitting the images into "red," "green," and "blue" components, a single camera simultaneously captures independent images of each laser sheet. Cameras are synchronized using a flashed light at the beginning or end of each experiment.

Images are processed by converting video files into sequences of RGB TIF images. The color of interest, e.g., blue for the streamwise vertical plane, is then extracted and corrected for lens and perspective distortions to create a distortion-free image or intensity map of the illuminated plane. Variations in illumination intensity are accounted for by treating each laser sheet as a set of five-point sources whose brightness decays linearly with distance. The streamwise vertical plane is captured by up to four cameras, and images from those cameras are stitched together to create a single image stack; no stitching is required for the horizontal and cross-stream planes as only one camera captures those planes. As the image intensity at any position is controlled by the number of particles reflecting the laser sheet at that position, intensity is a proxy for particle concentration.

Two-dimensional velocity fields are derived from the image sequences using a feature-tracking velocimetry (FTV) algorithm written for Matlab®. That algorithm compares a square region of a certain size located at a position in one image with the same size region located at the same position in the next image in the sequence captured 1/30 s later. Cross-correlation of those two regions describes motion within the region of interest between the two frames. This technique is similar to particle image velocimetry (PIV) except that the algorithm tracks larger-scale features rather than individual particles (the particles are smaller than the camera pixels). It should be noted that this algorithm only measures the 2D components of the 3D velocity field that lie within the laser sheet of interest, and the technique requires concentration gradients with length scales smaller than the interrogated region.

Vorticity fields, ω, are calculated as the curl of the FTV fields, u, at each position (x,y) as follows:

$$\omega(x,y) = \times\ u(x,y) = \frac{\partial u_y(x,y)}{\partial x} - \frac{\partial u_x(x,y)}{\partial y}$$

where x increases in the streamwise direction and y increases in the cross-stream or vertical direction (note that as flow is from right to left, these axes describe a left-handed coordinate

system). Because the vorticity fields are derived from the FTV data, the vorticities at any instant are very sensitive to noise within the underlying velocity data. Consequently, this paper presents vorticity fields calculated using linear least squares fits across 3×3 and 5×5 domains of FTV points averaged over 0.1 to 0.5 s; those intervals and length scales are sufficient to reduce noise without obscuring the transient nature of the turbulent flow fields.

Entrainment, E, is calculated as the ratio of the characteristic cross-stream and streamwise velocities, U_{cross} and U_{stream}, along the current margins and describes the rate at which fluid is entrained into the current.

$$E = \frac{U_{cross}}{U_{stream}}$$

The characteristic streamwise velocity is calculated as the mean streamwise component of velocity within the central portion of the current (for plan view projections) or within the basal portion of the current (for cross-sectional projections). The characteristic cross-stream velocity is determined as the mean of the cross-stream velocity components directed into the current. For example, in map view projections, the cross-stream velocity along the right side of the current is calculated as the sum of all left-directed velocity components divided by the total number of FTV points within that region. As a result,

entrainment is determined for the top, left, and right sides of the currents. It should be noted that this expression for E is slightly different than standard formulations (e.g., Turner 1986). Those formulations assume that the entrainment in the plane of observation produces increases in thickness or width within that plane; as will be shown in the "Results" section, 3D systems with reversing buoyancy do not necessarily behave in that manner; thus, standard formulations for entrainment do not work with the collected data.

Experimental scaling

Experiments are scaled such that bulk and turbulent scaling parameters are dynamically similar to those of natural dilute PDCs; the scaling follows that presented by Andrews and Manga (2011, 2012). Scaling relations are considered that account for the behavior of the entire current, coupling between the fluid and particles composing the current, and the thermal contrast between the current and the atmosphere. Bulk scaling parameters include Reynolds, densimetric and thermal Richardson, and Froude numbers, and the ratio of the thermal to kinetic energy density (Table 1). Turbulent scaling is monitored with the Stokes and Settling numbers (Table 1).

Comparison of the experiments with natural dilute PDCs shows that the two groups of currents are dynamically similar with respect to all scaling parameters except Reynolds (Re)

Table 1 Experimental scaling following the methods of Andrews and Manga (2011, 2012)

		Natural dilute PDCs	Experiments	Description
Re	$\frac{\rho_c U h}{\mu}$	10^6–10^9	10^3–10^4	Ratio of turbulent to viscous forces
Ri	$\frac{\rho_c g h}{\rho_{atm} U^2}$	0–10	0–20	Stratification stability. Stable stratification (Ri>10); unstable stratification (Ri<1); transitional behavior (1<Ri<10)
Ri_T	$\frac{g \Delta T a h}{U^2}$	0–5	0–5	Ratio of buoyant to forced convection. Forced convection dominates (Ri_T<0.1); buoyant convection dominates (Ri_T>10); combination of buoyant and forced convection (0.1<Ri_T<10)
Fr	$\frac{U}{\sqrt{g'h}}$	~1	~1	Ratio of inertial to gravitational forces
S_T	$\frac{\tau_v u'}{f \Lambda}\left(1+\frac{\rho_c}{2\rho_p}\right)$	0.01–200	10^{-4}	Coupling of particles to turbulent fluid motions. Complete coupling (S_T<1); complete decoupling S_T>1); clustering of particles along eddy margins (S_T~1)
$\sum_T$	$\frac{u_T}{u'}$	10^{-6}–10^5	<1	Ratio of particle settling velocity to turbulent fluctuations in velocity. Suspension ($\sum_T$<1); sedimentation ($\sum_T$>1)
KE	$\frac{\rho_c U^2}{2}$	10^3–10^4 J/m^3	10^{-3}–10^{-1} J/m^3	Kinetic energy density
TE_b	$\rho_c \frac{C_{p,curr}}{C_{p,atm}} g \Delta T a h$	10^3–10^4 J/m^3	0–10^{-1} J/m^3	Buoyant thermal energy density

Scaling is conducted with the Reynolds (Re), densimetric Richardson (Ri), thermal Richardson (Ri_T), Froude (Fr), Stokes (S_T), and settling ($\sum_T$) numbers, together with the kinetic and thermal energy densities (KE and TE_b). Atmospheric, particle, and current densities are denoted with ρ_{atm}, ρ_p, and ρ_c, respectively. Gravity and reduced gravity are abbreviated with g and g', where reduced gravity is defined as the product of gravity and the ratio of (ρ_c-ρ_{atm}) and ρ_{atm}. Current thickness is denoted with h, and the characteristic turbulent length scale with Λ. The difference between the initial current temperature and the atmosphere is ΔT, the coefficient of thermal expansion for air is given as a, and bulk heat capacities of the current and air are given as $C_{p,curr}$ and $C_{p,atm}$. The characteristic particle response time, τ_v, is determined following the technique described by Burgisser et al. (2005). f is a coefficient for particle drag, set to 1. The values of scaling parameters for natural dilute PDCs are from Burgisser et al. (2005), except for the Froude number, Fr, that is taken from scaling analyses of natural density currents (e.g., Simpson 1997). Supplementary Material 1 presents a schematic current illustrated with characteristic length scales and velocities

(although thermal energy (TE$_b$) and kinetic energy (KE) differ between the two groups of currents, the ratios of thermal to kinetic energy density are similar). The difference in Re scaling is a direct result of both sets of currents occurring with air as the ambient fluid: for experimental currents in air to have the same Re scaling as a natural PDC, they would need to be as thick, fast, and dense as natural PDCs. Fortunately, analysis of the experimental currents shows that they are fully turbulent; thus, although they have lower Re than the natural system, the largest scales of motion in the experiments are dynamically similar to the largest features in natural PDCs.

Results

Movies of experimental currents are presented in Supplementary Material 2 and 3. Experimental run parameters and results are summarized in Table 2.

Ambient temperature experiments appear similar to "classic" models of density currents. In cross section, the currents have the appearance of typical density currents, with well-developed heads followed by Kelvin-Helmholtz instabilities

on their upper surfaces (Fig. 2). As the currents flow, the heads generally increase in thickness. The lower halves of the currents typically move much faster than the upper portions, which often have almost no net forward velocity. That lower "bypass" region generally moves faster than and supplies the current head. The cross-stream and horizontal laser sheets show that the "classic" density current profile is present in all dispersal directions and the currents disperse radially from the inlet (Fig. 3). Occasionally, although the currents are supplied by a steady mass input rate, a single current with well-developed head and body will split into leading and trailing currents, each of which comprises a head and body (Fig. 2).

Experiments at elevated temperatures initially appear similar to the ambient temperature currents with well-developed heads. Soon after entering the tank, however, the thicknesses of the warm currents increase, and the currents lift off (Fig. 2). Once liftoff begins, the currents focus along a narrow dispersal axis beneath the rising plumes. As the currents continue, they feed directly into the rising plumes. The forward edges of the plume base do not continue to advance but instead define the maximum runout distance of the currents; the liftoff position does

Table 2 Experimental run conditions

Experiment	Mass (g)	Duration (s)	Rate (g/s)	ΔT (°C)	h_{head} (cm)	h_{body} (cm)	U_{head} (cm/s)	Re	Ri	Ri$_T$	TE$_b$/KE
20130625-1	40.8	100	0.408	0	32	17.78	23.4	2,574	4	0	0
20130625-2	17.8	100	0.178	0.00	24	12.7	15.2	1,184	3	0.0	0.0
20130625-3	17.5	100	0.175	0.00	15	7.6	11.7	549	3	0.0	0.0
20130625-4	19.6	31	0.632	0.00	17	10.2	21.9	1,399	4	0.0	0.0
20130625-5	18.7	31	0.603	0.00	32	16.5	25.4	2,615	5	0.0	0.0
20130627-1	33.9	570	0.059	0.00	30	12.7	5.2	401	11	0.0	0.0
20130627-2	13.6	540	0.025	0.00	31	12.7	9.4	718	1	0.0	0.0
20130627-3	72.1	600	0.120	0.00	20	10.2	7.2	449	8	0.0	0.0
20130711-1	126.3	50	2.526	0.00	40	22.0	30.5	4,576	17	0.0	0.0
20130715-1	65.8	31	2.123	0.47	42	20.3	22.2	3,131	29	0.8	1.8
20130715-2	58.1	31	1.874	0.96	35	20.3	24.4	3,352	18	1.1	2.1
20130716-1	60.6	100	0.606	1.88	33	17.8	40.6	4,442	2	0.7	1.3
20130716-2	33.8	300	0.113	2.83	37	20.0	5.9	735	19	58.2	2.5
20130716-3	66.8	300	0.223	1.23	25	12.7	8.1	647	14	9.2	1.4
20130716-4	44.4	100	0.444	1.23	25	11.4	10.6	776	16	5.4	2.2
20140322-2	45.1	31	1.437	0.00	25	12.0	39.3	6,708	3	0.0	0.0
20140322-3	27.2	300	0.091	0.00	30	11.0	12.2	2,391	3	0.0	0.0
20140322-6	16.9	300	0.056	0.1	20	11	9.4	1,223	2	0.4	0.3
20140322-7	7	300	0.023	0.35	18	10	6.4	751	2	3.0	2.1

Current mass is determined as the difference between initial mass loaded onto the conveyor belt and the "dead" mass at the base of the chute following each experiment. Duration is interval over which powder is supplied by the conveyor to the tank. ΔT is the difference in temperature between the current and the atmosphere in the tank. Thicknesses of the head and body, h_{head} and h_{body}, are measured at a distance of 1.25 m from the inlet; note that h_{head} often grows substantially during transport and h_{body} can be variable. The head velocity, U_{head}, is determined along the centerline at a distance of 1.25 m from the inlet. The Reynolds (Re), densimetric Richardson (Ri), thermal Richardson (RiT), and thermal to kinetic energy ratio (TE$_b$/KE) are determined based upon current parameters at a distance of 1.25 m from the inlet

Fig. 2 Time series of **a** ambient temperature (20130625-1, *left*) **b** heated (20130716-4, *right*) currents as illuminated by the streamwise vertical laser sheet. The two currents have comparable eruption rates (0.4 g/s) and durations (100 s) but different thermal to kinetic energy ratios (0 compared to 2.2). Ambient temperature currents comprise a well-developed head and body that persist throughout the length of the tank. The ambient temperature current splits into a leading and trailing current at 60–70 s. The heated current initially comprises a head and body, but by 30 s, the head is lifting off to form a buoyant plume that continues to rise for the duration of the experiment
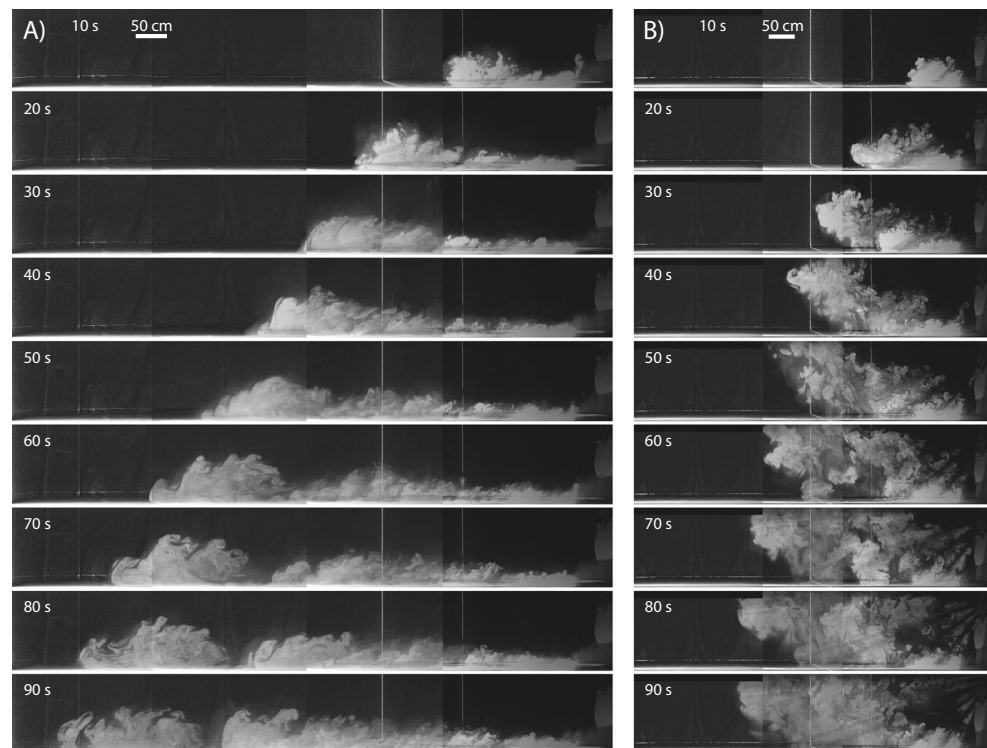
move slightly back and forth in the cross-stream direction. Plume rise occurs from the current fronts and tops. Although the most vigorous portion of the plume occurs near the current terminus, elements also rise from the body. The lower portions of heated currents form bypass regions similar to those seen in the ambient temperature experiments, with fast flow rates that feed the slower moving current head and/or rising plume. Map view images show that mixing with ambient air occurs along the lateral margins of the currents throughout experiments, and becomes particularly vigorous when liftoff begins (Fig. 3 and Supplementary Material 3).

Increases in experiment duration or mass flux produce interesting results but do not change the fundamental differences between ambient temperature and heated experiments. Increased "eruption" duration results in longer intervals over which both types of current transport and deposit particles (and, in the case of warm currents, evolve buoyant plumes). Anastamosing transport patterns are prevalent in most currents and manifest at a variety of timescales. Large, vertically-oriented vortices can span much of the width of heated currents, and those structures redirect the local flow field as they move through the currents. At longer timescales, the current centerlines typically sweep gently back and forth over a restricted or focused region (Supplementary Material 3). Heated currents with elevated mass flux exhibit an initially radial dispersal, but as soon as liftoff begins, the currents focus into a narrow dispersal axis.

Current dispersal and thickness

Ambient temperature currents vary in thickness from approximately 15 to 40 cm; thickness increases with current mass flux (Table 2). The current heads are typically thicker than the current bodies by a factor of ~1.5–3. Plots of the current head position versus time show that distance from the inlet increases approximately with the square root of time (Fig. 4). The areas inundated by the currents also increase through time, in this case with an approximately linear relationship (Fig. 4). The relationships of position and area with respect to time are consistent with one another. The aspect ratio of current dispersal, defined as the square of distance divided by area, initially increases as currents enter the tank, but stabilizes at a ratio of ~1.5–2 until currents interact with the sides of the tank, at which times the aspect ratios gently increase (Fig. 4).

Currents with elevated temperature vary in thickness from 18 to 42 cm, with thicknesses increasing with mass flux. The current heads are thicker than the current bodies by a factor of 1.5–2.5. When lift off occurs, the current heads feed directly into the rising plumes and the thickness of the current bodies increases as portions lift off. The current front positions increase approximately with the square root of time until liftoff occurs and the fronts becomes effectively stationary (Fig. 4). The areas inundated by the currents increase linearly with time until liftoff occurs, at which times the areal coverage stabilizes (Fig. 4). The current aspect ratio initially increases to values of

Fig. 3 Horizontal views of ambient temperature (*top*) and heated (*bottom*) currents. Current 20130625-1 at **a** 20 and **b** 50 s; the current spreads radially and extends through much of the tank. **c** Heated current 20130716-4 that initially spreads radially, albeit at a slower rate than 20130625-1. **d** At 50 s, ~25 s after liftoff, the current occupies a narrow region and shows focused dispersal along that axis
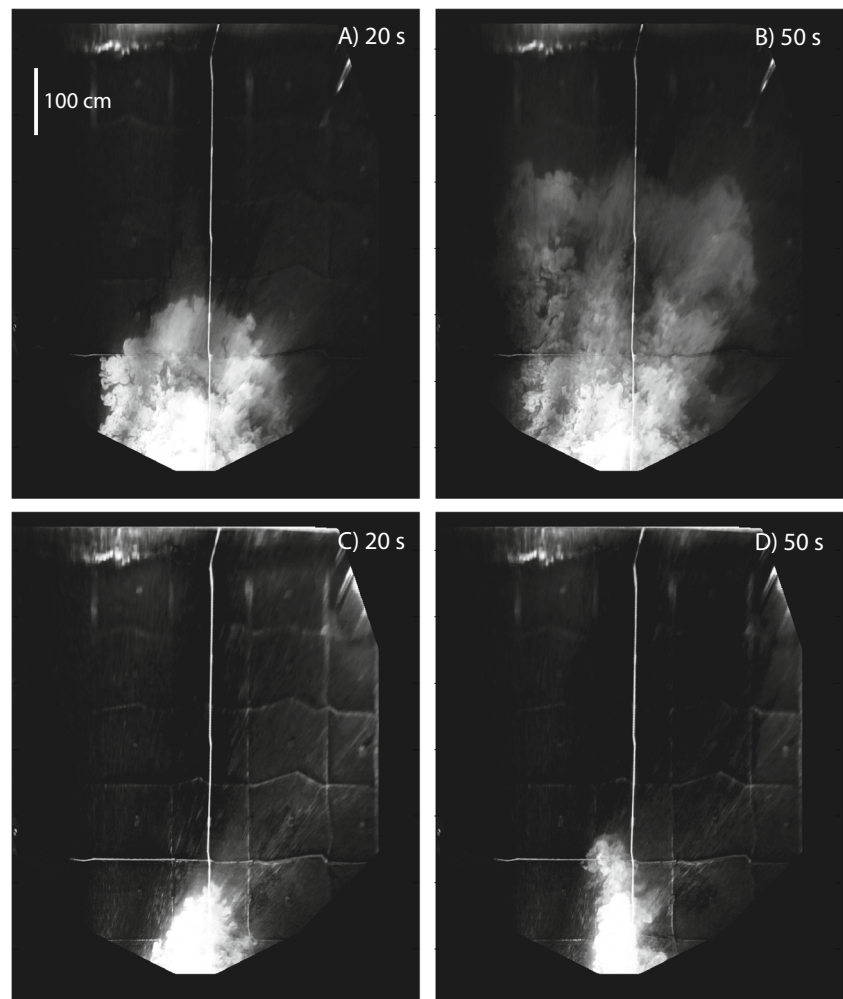
~3.5, and then stabilizes at values of 2.5–3.5 as the currents lift off and feed rising plumes (Fig. 4).

Increases in eruption rate or duration extend the runout distances and inundation areas of ambient temperature and heated currents (Fig. 4). Increases in eruption rate do not affect the aspect ratios of ambient temperature currents but result in decreases in the aspect ratios of heated currents.

Velocity fields

Feature tracking velocimetry shows that the velocity fields for all currents are turbulent with complex variation through time and space. In general, the highest velocities are measured near the inlet, although that region frequently has zero-value velocities resulting from saturated pixels and a lack of features for FTV analysis. The best FTV resolution appears in regions with strong fluctuations in image intensity (e.g., vigorous mixing).

Velocities in the vertical streamwise plane of ambient temperature currents are locally as high as 30 cm/s, with the fastest velocities in the lower half of the current bodies (Fig. 5). The

upper portion of the current heads and the upper margin of the current bodies often show upstream-directed velocities. Length scales and timescales of variation in velocity are measured from the 2D FTV velocity fields as the scales over which spatial or temporal correlation in velocity falls to zero (e.g., Andrews and Manga 2012). Velocities vary over a range of length and timescales, but the largest and most persistent features have scales as large as 20 cm and 3–5 s in the heads and ~10 cm and ~3 s in the bodies. Velocities measured in the horizontal plane show similar maximum amplitudes (up to 30 cm/s) and are on average directed radially outward from the inlet. The largest structures in the horizontal plane vary over timescales of several seconds and have length scales of 20–30 s; those scales are typically larger near the current fronts.

Velocity fields of heated currents are initially similar to ambient temperature currents, with highest velocities in the lower halves of currents. Velocities in the lower bypass zone of the bodies are commonly as high as 30 cm/s and are dominantly directed downstream, whereas those in the upper portions of the currents are much less steady in direction but can be as high as 30 cm/s (Fig. 5). When liftoff occurs, the

Ambient Temperature   Heated
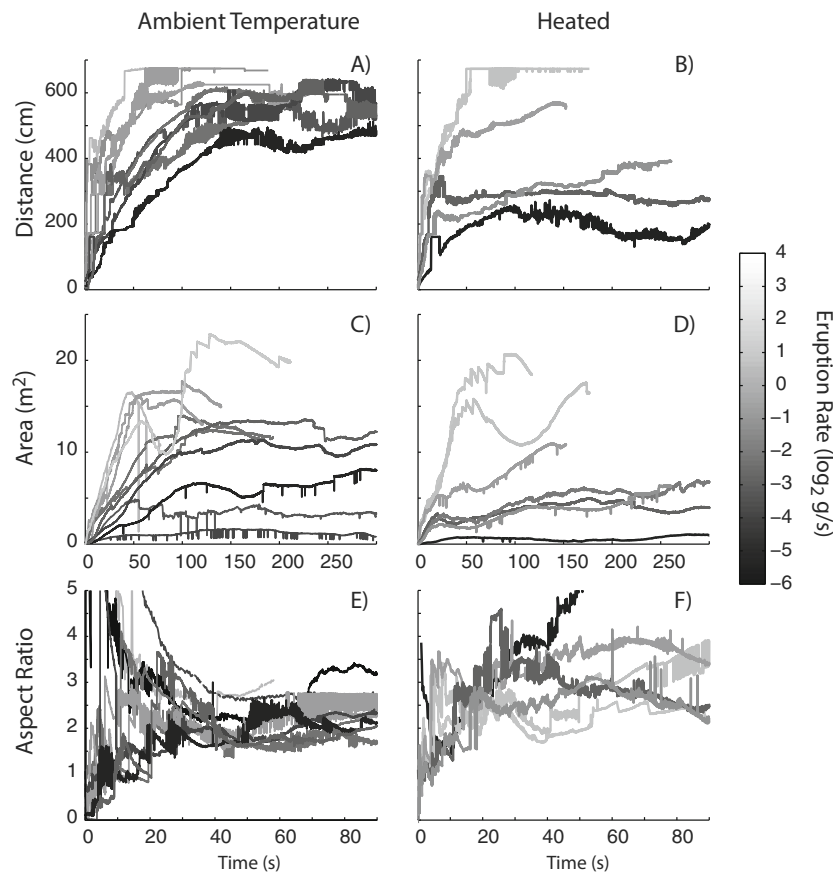
Fig. 4 Plots of distance, area, and aspect ratio versus time as measured in the horizontal plane. **a** Ambient temperature currents increase in distance with approximately the square root of time; the rate increases with the eruption rate. **b** The dispersal distance of heated currents also increases with eruption rate, but propagation is arrested when liftoff occurs. Note that the increase and plateau at 5–10 s in the lowest curve is the result of noise in the measured signal. **c** Inundation area increases with eruption rate for ambient temperature currents. **d** Inundation is largely arrested when liftoff occurs in heated currents. **e** The aspect ratios of ambient temperature currents generally stabilize at values of 1.5–2.5. **f** The aspect ratios of heated currents stabilize at values of 2.5–3.5 when liftoff occurs and dispersal focuses beneath the rising plumes; the aspect ratio of heated currents decreases with increasing eruption rate. Liftoff of the heated currents occurs at 20–25 s

velocity fields become more complex, commonly varying over length scales of ~10 cm. Although the lower portions of the current bodies are still directed primarily downstream, the rising plumes and upper portion of the bodies can move in all directions. Velocities measured in the horizontal plane show that the currents generally comprise a downstream-directed core with high velocities (up to 30 cm/s) and lower velocity margins. Velocities vary over length scales of 20–30 cm and timescales of ~3 s, with occasional ~50 cm structures that persist for as long as 10 s advecting downstream through the currents.

Vorticity fields

Vorticity fields measured in ambient temperature currents along the streamwise vertical plane show common structures. Regions of positive vorticity (clockwise rotation), approximately half to two thirds as thick as the heads, are present along the back of the current heads. Those regions comprise

many ~10-cm scale vortices that are in turn advected into the current heads. Individual vortices generally persist for <5 s and have intensities of 0.3–1.0/s. The bodies are characterized by 2–5-cm vortices. Vortical structures along the upper margin are often nearly motionless, whereas those deeper in the current are advected downstream. Structures near the upper margin tend to have positive vorticity (although numerous negative vorticity, or anti-clockwise, structures are also present), whereas structures near the base of the current often have negative vorticity.

Map view vorticity fields for ambient temperature experiments comprise approximately 10–20-cm vortices with intensities as high as 2/s that are advected outward through the currents (Fig. 6). No persistent or large-scale systematic structures are present. As the vast majority of those vortices are in the current interiors, they do not appear to enhance entrainment and mixing with the ambient air.

Vertical, streamwise vorticity fields of the heated currents are initially similar to the ambient temperature currents, with

Fig. 5 Representative feature tracking velocity vectors for ambient temperature (20130625-1) and heated (20130716-4) currents. **a** Ambient temperature currents have well-defined heads and bodies with the highest velocity regions generally in the lower half of the currents. **b** The bypass zone is apparent at 50 s as a consistently downstream-directed region near the base of the current. **c** By 20 s, the heated current has a very thick head that is generally flowing downstream, although large billows on the upstream side are directed in the opposite direction. **d** The velocity field is very complex in the current and rising plume. Velocity vectors shown are from FTV fields averaged over 1-s intervals
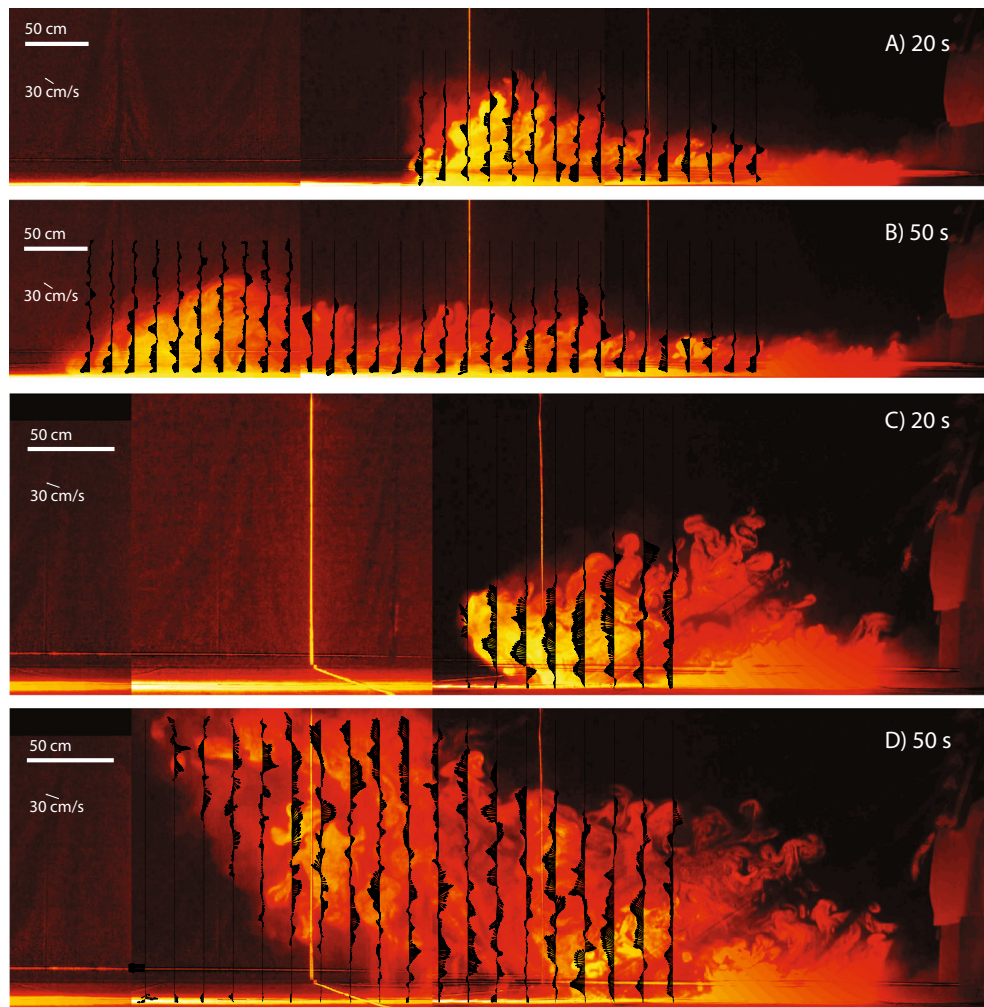
Fig. 6 Horizontal vorticity fields of ambient-temperature (20130625-1) and heated (20130716-4) currents. **a**, **b** The ambient temperature current vorticity fields show little structure and are characterized by small scale features. **c**, **d** The heated currents have well-organized vorticity fields characterized by persistent regions of positive (clockwise) vorticity on the right and negative vorticity on the left
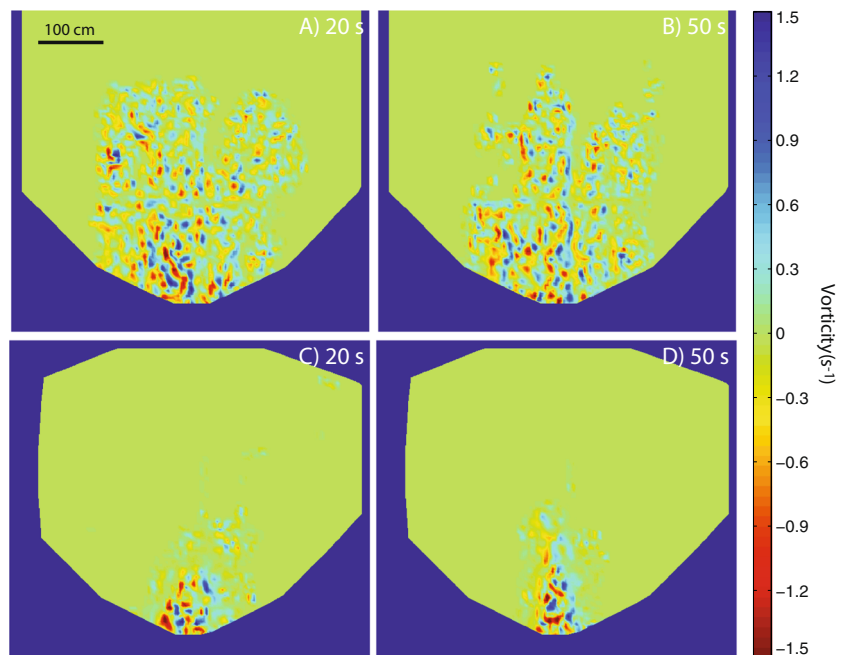
regions dominated by positive vorticity occurring behind and advecting into the heads. Those vortices are characterized by length scales of ~5 cm and intensities up to ~1.0/s. Once liftoff begins, the vorticity fields become less organized, with structures rising from the current to join the plume; those vortices are characterized by length scales of ~5 cm and intensities generally <0.7/s with no systematic orientation. Occasionally, a region of dominantly positive vorticity forms and is advected downstream into the most vigorous portion of the plume.

Horizontal vorticity fields of the heated currents show common and systematic structures. The vorticity fields become well organized as liftoff begins, with positive (clockwise) structures along the right margins of the currents and negative structures along the left margins (Fig. 6). The vortices commonly have intensities up to 2/s and length scales as large as 30 cm. Vortices along the current margins are generally advected downstream and persist for several seconds, although occasional structures stall and persist along the current margins. As vortices move downstream, they often migrate across the centerline. Near the liftoff position, the vortices are less persistent, and the left-right negative-positive structure of the currents decays. Short-lived vortices are commonly advected upstream in regions of backflow near the end of the current and along the current margins beneath the rising plume.

Entrainment

Entrainment occurs primarily through the upper margins of ambient temperature currents. Entrainment can be as high as ~0.3 behind the head and is typically ~0.10 in the body (Fig. 7), consistent with classical values (e.g., Wells et al. 2010). Because the current bodies are volumetrically much more significant than the current heads, the bodies dominate the total entrainment rates, particularly in long-duration currents. It should be noted, however, that as eddies on the upper margin of the bodies frequently do not penetrate into the bypass portion of the currents. Thus, entrainment through the upper margin and into the body may not be important for the current dynamics. Very little entrainment occurs through the lateral margins of the currents as their radial spread produces comparatively little shear across those margins.

Heated currents show complex variation in entrainment through space and time. Initially, entrainment is as high as ~0.3 behind the current heads, and entrainment in the bodies is ~0.1–0.15. When liftoff begins, however, vertical entrainment in the vicinity of the head falls to zero as the plume rises, and bulk entrainment into the body becomes very unsteady, frequently decreasing to zero as structures lift off from the body into the rising plume (Fig. 7). Entrainment through the current margins is unsteady prior to liftoff but increases through both
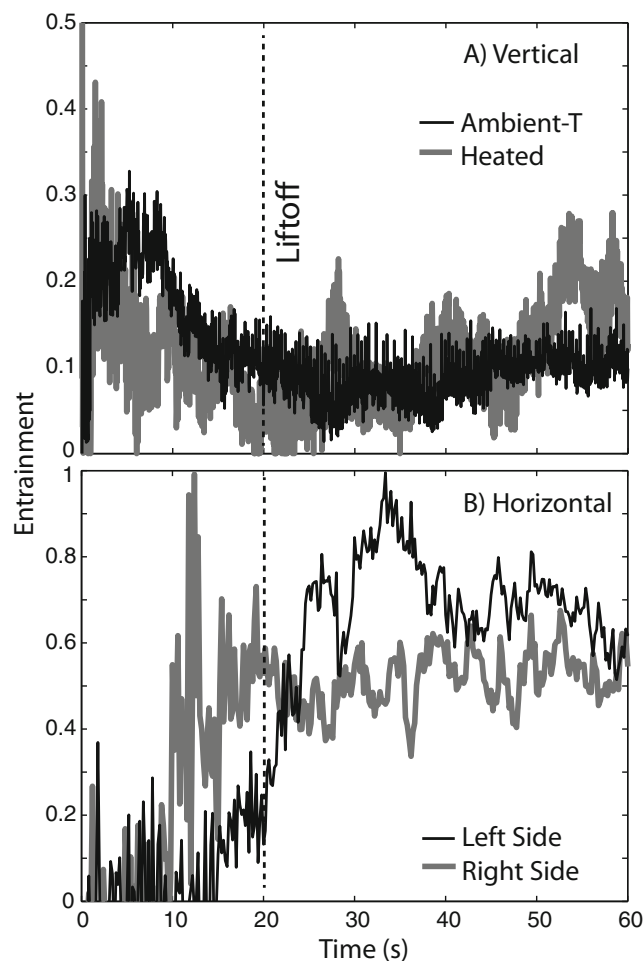
Fig. 7 Bulk entrainment for ambient temperature (20130625-1) and heated (20130716-4) currents. **a** Vertical entrainment through the upper current margins shows initially similar structures for the two currents, with high values when the head dominates behavior. As the body becomes more volumetrically important, the bulk entrainment rate for the ambient temperature current stabilizes at ~0.1. In contrast, as liftoff begins, vertical entrainment becomes very unsteady in the heated current, even dropping to 0. **b** Lateral entrainment into the heated current becomes very efficient when liftoff occurs at ~20 s, with values >0.5. Differences in the entrainment through the right and left side reflect local differences in turbulence, and development of a large eddy with negative vorticity near the left side of the current terminus at ~40 s

lateral margins to >0.5 when liftoff begins (Fig. 7). Those high rates persist through the durations of the currents.

Discussion

Two primary differences are apparent between ambient temperature and heated currents. First, heated currents evolve buoyant plumes, arresting further forward propagation of the current heads, whereas ambient temperature currents do not lift off but continue to propagate. The observations of ambient temperature currents are in agreement with numerous

previous studies (e.g., Bursik and Woods 1996), but the behavior of heated currents deviates from those works. Second, heated currents transport particles along focused sectors resulting in narrow dispersal patterns, whereas ambient temperature currents spread more radially and have broad dispersal patterns. The narrow dispersal of heated currents is a new observation that has implications for understanding and predicting the behavior of PDCs and their resulting deposits.

The narrow dispersal patterns of heated currents are a direct result of liftoff. Once buoyancy reversal occurs and liftoff begins, the conditions into which the density current flows change. Whereas the current initially flowed into a region with effectively still ambient fluid, a rising plume is now present above the density current. Continuity dictates that the rising plume imparts an upward-directed flow field onto the current's upper margin. That upwelling flow prevents the current from spreading laterally. This 3D effect is similar to the flow reversals following liftoff in 2D experiments described by Andrews and Manga (2012). It should also be recognized that the presence of the plume above the current inhibits air entrainment through the upper surface; thus, ambient fluid entrainment into the density currents is not constant but changes in response to current behavior.

Air entrainment through time and space

All density currents that undergo buoyancy reversal and liftoff spend time in three regimes of behavior: "pre-liftoff," "syn-liftoff," and "termination" (Fig. 8). Density currents that do not lift off (e.g., ambient temperature currents) exhibit behavior from the first and third regimes. Here, it should be noted that ambient temperature currents dominantly entrain air through their upper surfaces (behind the current head and via Kelvin-Helmholtz instabilities), whereas entrainment through the lateral margins dominates when liftoff occurs.

Pre-liftoff behavior occurs during the initial stages of current transport, when bulk current density is greater than that of the ambient fluid. The velocity field is turbulent, but the average flow field is away from the source. Entrainment behind the head and through the top of the body dominates during this phase. Peak entrainment can locally exceed 0.2 immediately behind the head, where a system of eddies efficiently mixes air into the moving current. For the bulk current, however, entrainment through the upper surface is 0.10–0.15; Kelvin-Helmholtz billows that are smaller and less energetic than the big vortex behind the head, account for this entrainment. These observations of entrainment are in general agreement with previous studies of entraining density currents that do not reverse buoyancy (e.g., Dade and Huppert 1995b; Wells et al. 2010). Lateral entrainment is relatively unimportant as these currents spread radially.

The basal, or bypass, region of the currents is the portion of the currents that lies below the reach of the Kelvin-Helmholtz
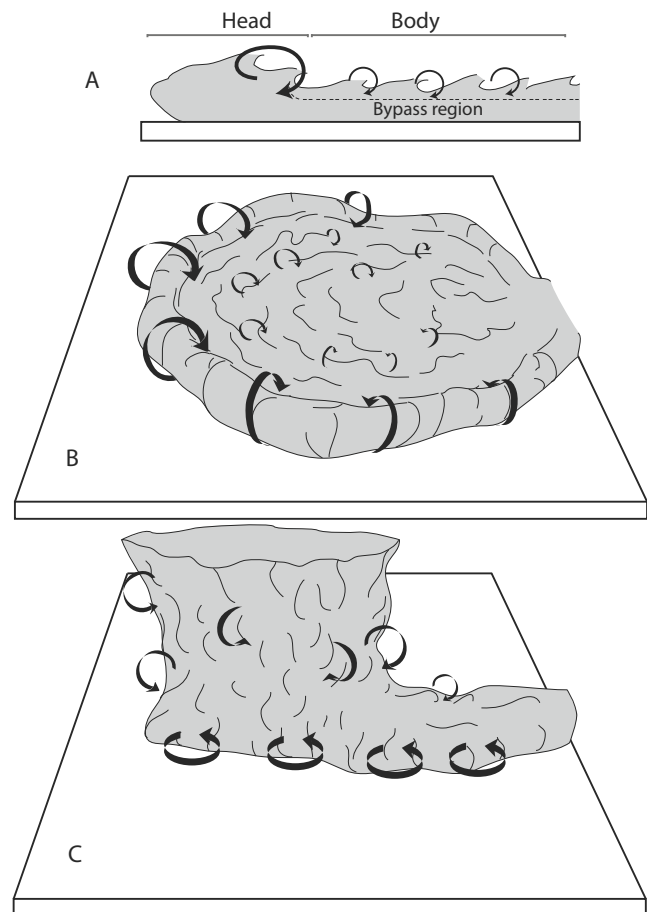
Fig. 8 Cartoon of density current structures with entrainment schematically shown by *curled arrows*. **a** "Classic" model of a density current, with entrainment highest immediately behind the current head. Entrainment through Kelvin-Helmholtz instabilities on the top of the body is largely restricted to the upper half of the body, leading to development of a "bypass region" that feeds the head with comparatively unmixed current. Deposits resulting from this type of current should have radial dispersal. **b** The classic density current model can be rotated about a vertical axis to create a reasonable model of 3D behavior of ambient temperature and pre-liftoff heated currents. **c** When buoyancy reversal begins, a plume forms above the current. That plume draws the current upward, preventing lateral spread of the current and thus focusing the current along a narrow axis. Entrainment along the upper margin is inefficient, but entrainment through vertically oriented vortices along the lateral margins is very efficient. Deposits from this type of current should be concentrated along the transport axis

billows and is thus below the mixing interface. As those bypass regions feed the heads, the cores of the current heads comprise comparatively unmixed or pristine parcels of the density currents. These observations suggest that development of multiple pulses from a single current (Fig. 2) occurs when mixing penetrates to the base of the current, disrupting the supply of material to the head; the stalled supply piles up to form a second, trailing head.

Syn-liftoff behavior occurs when portions of the current reverse buoyancy to form a plume. The velocity field changes as liftoff begins, reflecting plume rise and the imposition of an

upward-directed flow field on the bulk current. Although horizontal average velocities near the centerline remain directed away from the source, velocity vectors near the lateral margins of the currents redirect toward the centerline as liftoff begins. That inward-directed flow focuses the current along a narrow axis. Eddies generated by shear along the margins frequently penetrate and efficiently entrain air into the current interior. Flow reversals commonly manifest near the distal end of the current; reversals represent "true" backflow compared to a static point, not merely apparent backflow as compared to the current head. Those reversals are apparent in both map and cross-sectional views and likely result from the rising plume creating an upward flux greater than is supplied directly from the upstream current. Regions of backflow are fed by a combination of material shed by the rising plume and portions of the current that flow past or beneath the plume base without entraining enough air to become buoyant or be pulled into the plume.

During the syn-liftoff interval, when the density current feeds the rising plume, mixing between the current and ambient fluid is primarily restricted to the lateral margins of the currents. Lateral entrainment along each margin increases to >0.5 as liftoff begins. Entrainment occurs along both sides of the current; thus, net entrainment is some combination of entrainment through the right and left margins. Entrainment occurs primarily via large eddies on the current margins. The length scales of those structures are often comparable to the current width, and as those structures advect into the interior, they efficiently mix air into the current. Although individual eddies generally persist for only a few seconds and are not always advected the length of the current, persistent, vigorous mixing on the margins is indicated by the horizontal vorticity fields (Fig. 6).

Currents enter the termination phase when particle supply ceases. For ambient temperature currents, the head and body continue to move until all particles sediment. This phase of behavior for heated currents is marked by horizontal flow toward the plume base and liftoff of the entire current.

Application to natural PDCs

The experiments presented in this paper are dynamically similar to dilute PDCs. These experiments can both inform our general understanding of PDC behavior and help quantify specific processes. It should be noted that the experiments do not model all aspects of natural PDCs; for example, dense undercurrents are not present in these experiments, substrate erosion and entrainment does not likely occur, and nor does particle comminution and in situ generation of ash (Dufek and Manga 2008). Consequently, not all behaviors of natural systems are present in the experiments.

The experimental results suggest that when buoyancy reversal and liftoff occur in natural dilute PDCs, the currents

should focus upon comparatively narrow dispersal axes. Consequently, dilute PDCs should produce narrow, rather than broad, especially if liftoff and coignimbrite plume generation is sustained. To some extent, this prediction is borne out by observations of small-volume PDCs, such as some of the 1994 and 2010 surges at Merapi (Abdurachman et al. 2000; Cronin et al. 2013) that jetted out from the confining valleys before lifting off. PDC deposits from the Sovana eruption (Italy) show a total deposit with radial dispersal, but some facies occur as narrow lobes or sectors (Palladino and Taddeucci 1998); the restriction of facies D to the north and south of the vent could reflect liftoff and focusing of the current along those sectors. PDCs from the 1982 El Chichón (Mexico) eruption produced radial deposits extending ~10 km from the vent (e.g., S1) that are the product of numerous smaller, directed PDCs (Scolamacchia and Macías 2005). On the other hand, the S2 deposits at El Chichón have a radial occurrence that is interpreted to reflect radial dispersal, albeit to greater distances in the southeast (Scolamacchia and Macías 2005).

The deposits of large eruptions such as the 1.8 ka Taupo ignimbrite do not suggest focused dispersal Wilson (1985), and others have mapped those deposits throughout the North Island (New Zealand) and shown that the total deposit has an essentially radial dispersal. That dispersal pattern was used by Wilson to argue for very rapid transport and deposition by a single concentrated current in <400 s (Wilson 1985). Similarly, Dade and Huppert (1996) applied their analytical model to the deposits to infer deposition of the entire deposit over a period of ~15 min. Neither of those models for transport and deposition account for entrainment and liftoff of portions of the current. In addition, PDCs are now generally considered to deposit incrementally (Branney and Kokelaar 1992, 2002; thus, transport and depositional processes that last much longer, e.g., hours, are likely required to explain such large deposits. It should be noted here that even though large eruptions, such as that of Taupo, have different eruption mechanisms than the experiments, liftoff should still focus underlying dilute currents. That is, even if PDCs are generated with an initially radial dispersal in all directions, plume rise will focus the currents; in the case of a large eruption, multiple plumes might form along different dispersal azimuths, focusing current transport and deposition within discrete sectors beneath each plume like spokes on a wheel.

Several possible explanations exist for the disagreement between the experimental results and the dispersal patterns of large eruptions. First, the natural deposits could record deposition from numerous smaller volume PDCs with focused dispersal in different directions from the vent over relatively short time intervals, producing an aggregate radial deposit like the El Chichón S1 deposits (Scolamacchia and Macías 2005). Similarly, the transporting current, or currents, could have evolved numerous plumes that locally focused transport but whose durations were shorter than the response timescales of

the underlying depositional system (e.g., Andrews and Manga 2012); such a system would record the bulk radial dispersal and deposition without recording higher frequency or shorter wavelength processes. It is also possible that if the currents are generated as impulsive or short-duration currents, then there is little time for focusing to occur as the currents have small or non-existent bodies for the rising plume to act upon. Alternatively, the dynamics of truly radial eruptions of PDCs may be substantially different from the experiments (and initially focused or directed blasts and PDCs) such that the experimental results cannot be directly applied. For example, the eruption rate could be high enough that the radial, pre-liftoff phase of behavior is prolonged. Prior to liftoff, the most efficient air entrainment occurs behind the head and the bypass region of the body is largely isolated from entrainment. If the body supplies the head with a sufficient rate of "unmixed" current, the head could remain denser than the atmosphere, and thus, the current might not lift off. Similarly, truly radial dispersal could prevent efficient lateral entrainment during liftoff, because there are effectively no lateral margins or cross-stream interfaces between the current and ambient atmosphere for the entrainment to occur through. Both of those scenarios would prolong the pre-liftoff stage of behavior and prevent the more efficient air entrainment and focusing that occurs during the syn-liftoff phase. Lastly, the behavior of the natural currents could be dominated by dense undercurrents at the base of the PDC; experiments by Roche (2012) have demonstrated that granular flows can retain high pore-pressure for tens of minutes permitting flows >5 m thick to travel tens of kilometers. If present, thick granular flows should exert fundamental controls on current behavior and dominate the depositional system such that behaviors of the overlying dilute current, including focusing beneath plumes, are not recorded. Very likely, a combination of all of the above processes occurs in natural PDCs.

Conclusions

Laboratory experiments with dynamic scaling similar to natural dilute PDCs indicate fundamental differences between ambient temperature density currents and warm density currents that reverse buoyancy to form plumes. Ambient temperature currents spread radially and entrain air primarily behind the current head and through the upper surface of the current body. In contrast, although heated currents initially entrain air through similar structures, as soon as portions of the currents reverse buoyancy, rising plumes form above the currents. The presence of those plumes block most entrainment through the upper current margins and draws the currents inward resulting in dispersal along narrow axes with entrainment focused along the lateral margins. Entrainment through the lateral margins is

more efficient than entrainment behind the head or through the upper surface, >0.5 compared to 0.1–0.15. The experiments presented in this paper demonstrate that 3D structures and flow fields control the dynamics of dilute PDCs. These results suggest that 2D experiments and numerical models may not capture important transport and depositional processes and that some existing 3D numerical models may not properly describe entrainment and its effects on current dispersal.

References

Abdurachman EK, Bourdier JL, Voight B (2000) Nuees ardentes of 22 November 1994 at Merapi volcano, Java, Indonesia; Merapi volcano. J Volcanol Geotherm Res 100:345–361

Andrews BJ, Manga M (2011) Effects of topography on pyroclastic density current runout and formation of coignimbrites. Geology 39:1099–1102

Andrews BJ, Manga M (2012) Experimental study of turbulence, sedimentation and coignimbrite mass partitioning in dilute pyroclastic density currents. J Volcanol Geotherm Res 225–226:30–44

Branney MJ, Kokelaar P (1992) A reappraisal of ignimbrite emplacement; progressive aggradation and changes from particulate to non-particulate flow during emplacement of high-grade ignimbrite. Bull Volcanol 54:504–520

Branney MJ, Kokelaar BP (2002) Pyroclastic density currents and the sedimentation of ignimbrites. Memoirs of the Geological Society of London, London, 27. 143 pp

Burgisser A, Bergantz GW, Breidenthal RE (2005) Addressing the complexity in laboratory experiments: the scaling of dilute multiphase flows in magmatic systems. J Volcanol Geotherm Res 141:245–265. doi:10.1016/j.jvolgeores.2004.11.001

Bursik MI, Woods AW (1996) The dynamics and thermodynamics of large ash flows. Bull Volcanol 58:175–193

Bursik MI, Woods AW (2000) The effects of topography on sedimentation from particle-laden turbulent density currents. J Sediment Res 70:53–63

Cantero M, Cantelli A, Pirmez C, Balachandar S, Mohrig D, Hickson T, Yeh T-H, Naruse N, Parker G (2012) Emplacement of massive turbidites linked to extinction of turbulence in turbidity currents. Nat Geosci 5:42–45

Cronin SJ, Lube G, Dayudi DS, Sumarti S, Subrandinyo S, Surono (2013) Insights into the October-November 2010 Gunung Merapi eruption (central Java, Indonesia) from the stratigraphy, volume and characteristics of its pyroclastic deposits. J Volcanol Geotherm Res 261:244–259

Dade BW, Huppert HE (1995a) A box model for non-entraining suspension-driven gravity surges on horizontal surfaces. Sedimentology 42:645–648

Dade BW, Huppert HE (1995b) Runout and fine-sediment deposits of axisymmetric turbidity currents. J Geophys Res 100:18597–18609

Dade WB, Huppert HE (1996) Emplacement of the Taupo ignimbrite by a dilute turbulent flow. Nature 381:509–512

Dellino P, La Volpe L (2000) Structures and grain size distributions in surge deposits as a tool for modeling the dynamics of dilute pyroclastic density currents at La Fossa di Vulcano (Aeolian Islands, Italy). J Volcanol Geotherm Res 96:57–78

Dellino P, Buttner R, Dioguardi F, Doronzo DM, La Volpe L, Mele D, Sonder I, Sulpizio R, Zimanowski B (2010) Experimental evidence links volcanic particle characteristics to pyroclastic flow hazard. Earth Planet Sci Lett 295:314–320

Druitt TH, Calder ES, Cole D, Hoblitt RP, Loughlin SC, Norton GE, Ritchie LJ, Sparks RSJ, Voight B (2002) Small-volume, highly mobile pyroclastic flows formed by rapid sedimentation from pyroclastic surges at Soufriere Hills Volcano, Montserrat: an important volcanic hazard. In: Druitt TH, Kokelaar BP (eds) The eruption of Soufriere Hills Volcano, Montserrat, from 1995 to 1999, vol 21. Geol. Soc. Lond. Mem, London, pp 263–279

Dufek J, Bergantz GW (2007) Suspended load and bed-load transport of particle laden gravity currents: the role of particle-bed interaction. Theor Comput Fluid Dyn 21:119–145. doi:10.1007/s00162-007-0041-6

Dufek J, Manga M (2008) The in-situ production of ash in pyroclastic flows. J Geophys Res 113, B09207. doi:10.1029/2007JB005555

Esposti Ongaro T, Neri A, Todesco M, Macedonio G (2002) Pyroclastic flow hazard assessment at Vesuvius (Italy) by using numerical modeling. II. Analysis of flow variables. Bull Volcanol 64:178–191. doi:10.1007/s00445-001-0190-1

Esposti Ongaro T, Neri A, Menconi G, de'Michieli Vitturi M, Marianelli P, Cavazzoni C, Erbacci G, Baxter PJ (2008) Transient 3D numerical simulations of column collapse and pyroclastic density current scenarios at Vesuvius. J Volcanol Geotherm Res 178:378–396. doi:10.1016/j.jvolgeores.2008.06.036

Fisher RV, Orsi G, Ort MH, Heiken G (1993) Mobility of a large-volume pyroclastic flow—emplacement of the Campanian ignimbrite, Italy. J Volcanol Geotherm Res 56:205–220

Fujii T, Nakada S (1999) The 15 September 1991 pyroclastic flows at Unzen Volcano (Japan): a flow model for associated ash-cloud surges. J Volcanol Geotherm Res 89:159–172

Gardner JE, Burgisser A, Stelling P (2007) Eruption and deposition of the Fisher Tuff (Alaska): evidence for the evolution of pyroclastic flows. J Geol 115:417–435

Palladino DM, Taddeucci J (1998) The basal ash deposit of the Sovana Eruption (Vulsini Volcanoes, central Italy): the product of a dilute pyroclastic density current. J Volcanol Geotherm Res 87:233–254

Roche O (2012) Depositional processes and gas pore pressure in pyroclastic flows: an experimental perspective. Bull Volcanol 74:1807–1820. doi:10.1007/s00445-012-0639-4

Scolamacchia T, Macías JL (2005) Distribution and stratigraphy of deposits produced by diluted pyroclastic density currents of the 1982 eruption of El Chichón volcano, Chiapas, Mexico. Rev Mex Cienc Geol 22:159–180

Sigurdsson H, Carey S (1989) Plinian and co-ignimbrite tephra fall from the 1815 eruption of Tambora volcano. Bull Volcanol 51:243–270

Simpson JE (1997) Gravity currents in the environment and laboratory. Cambridge University Press, Cambridge

Stagnaro M, Bolla Pittalyga M (2013) Velocity and concentration profiles of saline and turbidity currents flowing in a straight channel under quasi-uniform conditions. Earth Surf Dyn Discuss 1:817–853. doi:10.5194/esurfd-1-817-2013

Todesco M, Neri A, Esposti Ongaro T, Papale P, Macedonio G, Santacroce R, Longo A (2002) Pyroclastic flow hazard assessment at Vesuvius (Italy) by using numerical modeling. I. Large-scale dynamics. Bull Volcanol 64:155–177. doi:10.1007/s00445-001-0189-7

Turner JS (1986) Turbulent entrainment: the development of the entrainment assumption, and its application to geophysical flows. J Fluid Mech 173:431–471

Wells M, Cenedese C, Caulfield CP (2010) The relationship between flux coefficient and entrainment ratio in density currents. J Phys Oceanogr 40:2713–2727. doi:10.1175/2010JPO4225.1

Wilson CJN (1985) The Taupo eruption, New Zeland II. The Taupo Ignimbrite. Phil Trans R Soc Lond Ser A Math Phys Sci 314:229–310

Wilson CJN (2008) Supereruptions and supervolcanoes: processes and products. Elements 4:29–34. doi:10.2113/GSELEMENTS.4.1.29

Woods AW, Kienle J (1994) The dynamics and thermodynamics of volcanic clouds: theory and observations from the April 15 and April 21, 1990 eruptions of Redoubt Volcano, Alaska. J Volcanol Geotherm Res 62:273–299